Biochemistry **2004,** *43,* 7017−7027

Proximal and Distal Influences on Ligand Binding Kinetics in Microperoxidase and Heme Model Compounds[†]

Wenxiang Cao, Xiong Ye, Georgi Y. Georgiev, Svitlana Berezhna, Theodore Sjodin, Andrey A. Demidov,
Wei Wang, J. Timothy Sage, and Paul M. Champion*

*Department of Physics and Center for Interdisciplinary Research on Complex System, Northeastern University,
Boston, Massachusetts 02115*

Received February 5, 2004; Revised Manuscript Received April 2, 2004

ABSTRACT: We use laser flash photolysis and time-resolved Raman spectroscopy of CO-bound heme complexes to study proximal and distal influences on ligand rebinding kinetics. We report kinetics of CO rebinding to microperoxidase (MP) and 2-methylimidazole ligated Fe protoporphyrin IX in the 10 ns to 10 ms time window. We also report CO rebinding kinetics of MP in the 150 fs to 140 ps time window. For dilute, micelle-encapsulated (monodisperse) samples of MP, we do not observe the large amplitude geminate decay at ~100 ps previously reported in time-resolved IR measurements on highly concentrated samples [Lim, M., Jackson, T. A., and Anfinrud, P. A. (1997) *J. Biol. Inorg. Chem. 2*, 531−536]. However, for high concentration aggregated samples, we do observe the large amplitude picosecond CO geminate rebinding and find that it is correlated with the absence of the iron-histidine vibrational mode in the time-resolved Raman spectrum. On the basis of these results, the energetic significance of a putative distal pocket CO docking site proposed by Lim et al. may need to be reconsidered. Finally, when high concentration samples of native myoglobin (Mb) were studied as a control, an analogous increase in the geminate rebinding kinetics was not observed. This verifies that studies of Mb under dilute conditions are applicable to the more concentrated regime found in the cellular milieu.

Heme proteins bind small diatomic ligands (CO, O_2, and NO) to fulfill their roles in respiration, signaling, and catalysis. The investigation of ligand binding kinetics is thus essential for the understanding of heme protein biological function. Numerous studies have been performed on the O_2-binding proteins, myoglobin (Mb),[1] and hemoglobin (Hb) (*1*−*4*), but due to the complexity of protein structure, function, and dynamics relationships, the detailed mechanism of ligand binding to these proteins is still not fully understood.

The shape, volume, and polarity of the distal heme pocket (where the diatomic ligand binds) can affect the migration and stability of the ligand when it binds (*3*−*12*). The distal histidine residue (His-64) plays a particularly significant role in discriminating between O_2 and CO by providing a much stronger hydrogen bond to O_2 (*12*−*18*). Moreover, His-64 probably plays the role of a "gate" allowing small molecules to enter or escape from the solvent-inaccessible ligand-binding site (*11*, *19*−*25*). The distal protein residues have also been proposed to form a docking site (*26*, *27*) that influences the geminate ligand rebinding rate by constraining orientationally and spatially the diatomic ligand (*28*−*30*).

On the other hand, the proximal histidine residue (His-93) binds directly to the iron and also influences the trans binding of diatomic ligands. Protein modulation of the heme affinity through the proximal linkage plays a central role in the Perutz mechanism for cooperative oxygen binding in hemoglobin (*31*, *32*). This modulation may involve control of the iron displacement perpendicular to the heme plane (*33*). In certain cases, a proximal ligand switch can influence the binding of diatomic ligands (*34*−*37*). Extensive work on model compounds (*38*−*42*) has also provided strong evidence for proximal effects on diatomic ligand binding (vide infra).

In previous work, we have quantitatively delineated energetic contributions to the rebinding barriers and partitioned them into proximal and distal terms, which were estimated to be roughly equal in magnitude (*33*). Nevertheless, it remains controversial which side (proximal or distal) plays the dominant role in diatomic ligand binding and in determining the distribution of barriers observed at low temperature (*2*, *3*, *36*, *43*−*51*). More specifically, the energetic significance of the putative "docking site" (*26*, *27*) remains unclear.

In this work, we use laser flash photolysis and resonance Raman spectroscopy to investigate the effects of the distal heme pocket on ligand rebinding. We probe the distal effects by examining samples of microperoxidase (MP) and 2-methylimidazole-ligated iron protoporphyrin IX [Fe(II)(PPIX)-(2-MeIm)] in detergent micelles, where the globular protein

---

[†] This work was supported by grants from NSF (0211816 and 0240955) and NIH (DK035090 to P.M.C. and GM-52002 to J.T.S.).

* To whom correspondence should be addressed. Champion, P. M.: E-mail: p.champion@neu.edu; tel. (617) 373-2918; fax: (617) 373-2943. Sage, J. T.: E-mail: jtsage@neu.edu; tel: (617) 373-2908; fax (617) 373-2943.

[1] Abbreviations: Mb, myoglobin; Hb, hemoglobin; MP, microperoxidase; MP(11), microperoxidase-11; MP(8), microperoxidase-8; Fe(PPIX), Fe protoporphyrin IX; 2-MeIm, 2-methylimidazole; CO, carbon monoxide; O_2, oxygen; NO, nitric oxide; CTAB, cetyltrimethylammonium bromide.

10.1021/bi0497291 CCC: $27.50

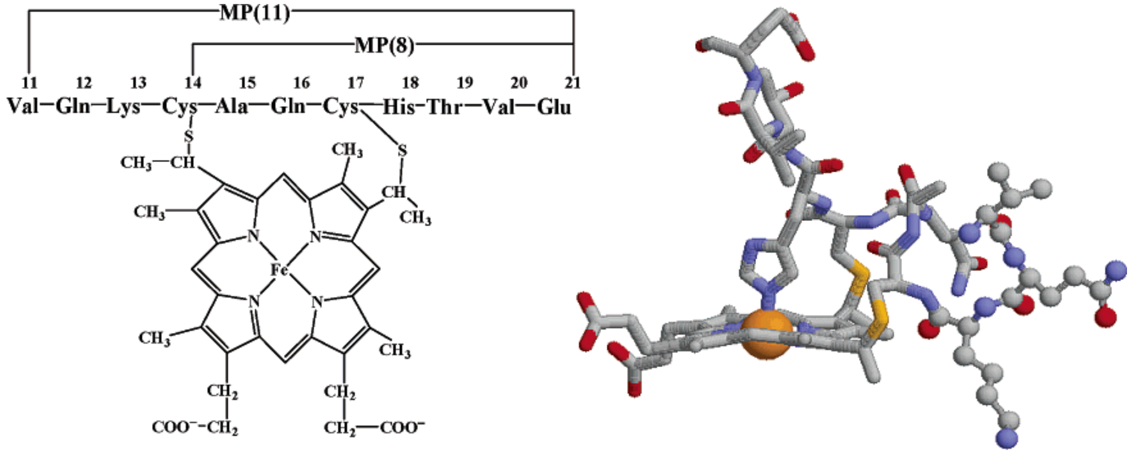

FIGURE 1: The structures of MP8 and MP11 showing the heme and the covalently attached amino acids (left). The 3D structure of the MP11 is also shown (right). The three extra amino acids in the peptide chain of MP(11) are shown in stick and ball models (right).

is partly or completely stripped away. Microperoxidase is prepared by enzymatic digestion of cytochrome *c* (*52*). As shown in Figure 1, MP has a "basket handle" peptide chain whose histidine binds to the heme iron and mimics the hemeprotein structure in absence of a distal pocket. There are two basic variants of MP: one with 11 amino acids, MP(11), and one with eight amino acids, MP(8). These structures are depicted on the left side of Figure 1 and a 3D representation of MP(11), based on the cytochrome *c* structure, is shown on the right (the three extra amino acids in the peptide chain of MP(11) are shown in stick and ball representation). When dissolved in detergent micelles, both the MP system and the Fe(II)(PPIX)(2-MeIm) compound mimic the heme protein structure in the absence of a specifically organized distal pocket.

Prior work, over a decade ago (*35*, *53*), established quite clearly that little or no CO geminate rebinding takes place in heme model compounds. This, along with detailed pH titrations involving the proximal histidine ligand (*34*, *39*, *54*), revealed that proximal ligation effects played a significant role in determining the barrier to CO rebinding. In contrast, the recent infrared studies of Anfinrud and colleagues (*29*, *30*) demonstrated a 90% geminate rebinding amplitude in the MP11 system and were interpreted as evidence that a distal pocket "docking site" plays an overwhelming role in determining the barrier to CO rebinding. In this study, we show that elimination of the putative distal "docking site" does not lead to the reported 10^5-fold increase in the geminate CO rebinding rate (*29*, *30*). In contrast, we observe that perturbations of the proximal heme ligand (associated with intermolecular interactions) are strongly correlated with the dramatic aggregation-dependent changes observed in the ligand rebinding kinetics.

EXPERIMENTAL METHODS

Sample Preparation. Horse heart myoglobin, microperoxidase-8 (MP(8)), and microperoxidase-11 (MP(11)) were purchased from Sigma Chemical Co. Horse heart myoglobin was prepared in 0.1 M phosphate buffer, pH 7. The MP(8) and MP(11) samples were prepared in pH 7, 0.1 M phosphate buffer with 1% (w/v) hexadecyltrimethylammonium bromide (cetyltrimethylammonium bromide, CTAB, also from Sigma). Fe(II)(PPIX)(2-MeIm) was prepared by dissolving hemin purchased from Aldrich Chemical Co. into 0.1 M phosphate buffer pH 8.5 with 0.1 M 2-MeIm and 1% (w/v) CTAB. (Unlike 1-MeIm, the methyl group in 2-MeIm sterically hinders the formation of the bis-2-MeIm complex so that competitive binding between CO and a second 2-MeIm ligand is not observed.) Typical sample concentrations for the kinetics measurements were 50−100 μM. The CTAB detergent present in the MP(8), MP(11), and Fe(II)(PPIX) sample solutions forms micelles that encapsulate the model compounds and inhibit aggregation (*55*, *56*). A highly concentrated MP(11) sample solution (2−15 mM) was used as a control and prepared in the same way, but without CTAB, to reproduce the condition used in previous IR experiments (*29*).

Nanosecond flash photolysis experiments were performed on samples with a concentration <0.1 mM prepared in cuvettes with a 1-mm optical path length. Samples were degassed by repeatedly evacuating the cuvette headspace and flushing with Ar gas. A small amount of degassed dithionite solution was used to reduce the samples. The CO adduct was formed from the reduced samples by flushing with CO for 30 min. Samples with a concentration <0.1 mM used for the ultrafast kinetics and Raman experiments were made in gastight vials in a similar way and were transferred into either a spinning sample cell with 1-mm optical path length for ultrafast kinetics or into a stationary 1-mm cuvette or 10-mm diameter cylindrical spinning cell for Raman experiments. High concentration (>1 mM) samples were prepared in vials in a similar way and transferred into a spinning sample cell with 15- or 50-μm optical path length for kinetics measurements.

Sample pH values were measured by a Beckman Instruments Φ40 pH meter. Sample static absorption spectra were obtained using a Hitachi U-3410 spectrophotometer.

Experimental Setup and Procedures. The laser flash photolysis experimental setup and procedures have been described in detail previously (*25*). Briefly, a cw beam produced by a universal arc lamp (Oriel Instruments, model 66021) and a 0.25 m monochromator (Oriel Instruments, model 77200) are used to probe the kinetic response of the sample at selected wavelengths. The signal is detected by a high-linearity, low noise, photomultiplier (Hamamatsu, H6780) and recorded by a transient digitizer (LeCroy 9420). A laser pulse (10 ns, 532 nm), produced by a 10 Hz Nd-doped yttrium−aluminum-garnet (YAG) laser (Continuum, Inc.), is used to photolyze the sample. The pump pulse energy is typically 25 mJ.

The ultrafast kinetics measurement setup and experimental procedure are described in detail elsewhere (*57*, *58*). An amplified 250 kHz Ti:sapphire laser (REGA 9050, Coherent, Inc.) system generates ∼50 fs laser pulses at ∼800 nm with an average power of ∼1 W. These fundamental pulses are used to pump an optical parametric amplifier (OPA, Coherent 9400) and to generate white light continuum. The white light continuum, which is used as a sample probe, is created by focusing the 800 nm fundamental into a spinning fused silica disk, and its spectrum extends from 390 to 800 nm. A monochromator (Triax 320, Spex) is used to disperse the probe light after the sample. The OPA (50 fs, 250 kHz) is also driven by the 800 nm fundamental and the resulting pulses, used to photolyze the samples, can be tuned from about 520 to 650 nm. The time delay for the probe (white light continuum) with respect to the pump (OPA pulse) is controlled using a precision translation stage (Melles Griot, Inc.). The pump and probe beams are focused into a specially designed spinning sample cell using an achromatic lens. The sample cell has a 2 in. diameter titanium frame that spins at a rate of over 7000 rpm to ensure that every pump−probe pulse pair detects fresh sample. This ensures that problems like thermal lensing and build-up of product state population are eliminated. Care was also taken to make the pump beam completely overlap the probe beam at the sample. The time resolution of 200 fs is determined by pump−probe cross-correlation. The kinetics measurements employ synchronous detection, where the pump beam is modulated by a mechanical chopper (3 kHz), and the pump-induced change in the probe signal is detected at each time delay using a PMT and a lock-in amplifier. Variations in probe power within the monochromator-selected bandwidth are compensated using a feedback circuit (*59*). Data points are displayed for $t \geq 600$ fs, after which the contribution from the coherence coupling and oscillations are negligible.

The cw resonance Raman setup and data processing have also been reported elsewhere (*60*). The excitation source is the 413.1 nm line generated by a Kr ion laser (Innova 300, Coherent, Inc.). Light scattered in the right angle geometry (90°) from the sample is collected by lenses and focused into a single grating monochromator (1870B, Spex Industries). An interferometric notch filter (Kaiser Instruments) rejects the intense Rayleigh scattered light. A liquid-nitrogen-cooled CCD detector (Princeton Instruments), interfaced to a personal computer, records the frequency-resolved intensity of the scattered light. The Raman spectra are calibrated using fenchone as a frequency standard, with a resulting 2 cm^{-1} frequency uncertainty.

The 10-ns transient resonance Raman setup (*61*) is similar to the cw resonance Raman setup. The excitation used to generate time-resolved resonance Raman spectra is derived from 10 ns, 532 nm laser pulses produced by a 10 Hz Nd:YAG laser (Continuum, Inc.) and a homemade 50-cm long Raman shifter filled with 185 psi high purity hydrogen gas. The resulting anti-Stokes shifted light results in 10-ns pulses at 435.8 nm. Care is taken to eliminate uneven stress on the 1-cm-thick quartz windows at both ends of the Raman shifter cell so that effects due to birefringence are reduced. Two watts of the 532 nm beam are focused with a 30-cm focal length lens into the Raman cell to generate ∼10 mW Raman shifted laser light at 435.8 nm. A dichroic mirror and a blue glass filter are used after the Raman shifter to filter out the 532 nm light and the first red-shifted Stokes line, respectively. The scattered Rayleigh light from the sample is attenuated at the monochromator entrance slit by a 442-nm interferometric notch filter (Kaiser Instruments) angle tuned to 435.8 nm. Depending on the details of the scattering geometry, three sharp additional lines sometimes appear in the time-resolved resonance Raman spectra, especially when high concentration samples are used or if the laser beam scatters off the cuvette surface. These spurious features are positioned at 237, 587, and 1084 cm^{-1} and, when necessary, are removed from the spectra.

Measurement of Rate Constants. A simple three-state kinetic model (*62*) that is widely used to describe the biphasic ligand rebinding process in heme proteins is

$$\text{MbCO} \xleftarrow[k_{\text{BA}}]{} \text{Mb:CO} \underset{k_{\text{in}}}{\overset{k_{\text{out}}}{\rightleftharpoons}} \text{Mb} + \text{CO} \qquad (1)$$

Here, MbCO is the CO-bound state, Mb:CO is an intermediate state with the dissociated CO in the distal pocket, and Mb+CO is the state when the photolyzed CO is in the solvent. Within this model, the absorption change as function of time can be expressed as (*62*)

$$\Delta A(t) = \Delta A_0 (I_g e^{-(k_g t)^{\beta}} + (1 - I_g)(1 - [\text{Mb}]/[\text{CO}])/ (e^{k_s t} - [\text{Mb}]/[\text{CO}])) = \Delta A_0 N(t) \quad (2)$$

with $0 \leq \beta \leq 1$. The absorbance change, $\Delta A(t)$, is proportional to the population of the ligand dissociated heme ($N(t)$) and ΔA_0 is used to normalize the data. The quantity I_g is the geminate rebinding amplitude, and k_g and k_s are rate constants for the geminate and bimolecular phases of rebinding, respectively. [Mb] is the initial concentration of photolyzed protein (and photolyzed CO) so that the total free CO concentration after photolysis is $[\text{CO}] = [\text{CO}]_{\text{eq}} + [\text{Mb}]$, in which $[\text{CO}]_{\text{eq}}$ is the equilibrium CO concentration dissolved in solvent prior to photolysis.

The relation between the fundamental rates defined in the three-state model (eq 1) and the observed rates in eq 2 is given by

$$k_{\text{BA}} = I_g k_g$$

$$k_{\text{out}} = k_g (1 - I_g)$$

$$k_{\text{in}} = k_{\text{on}} / I_g$$

$$k_{\text{on}} = k_s / ([\text{CO}] - [\text{Mb}]) \qquad (3)$$

where k_{on} is the CO concentration-independent bimolecular CO rebinding rate. When using eq 2 to fit the experimental data and eq 3 to calculate the fundamental rates, the total concentration of photolyzed protein, [Mb], has to be accurately determined. In the low concentration samples, [Mb] is calculated from $[\text{CO}]_{\text{eq}}$ (assuming ∼1 mM CO solubility in water (*63*)) and the value of [CO] found using eq 2). To accurately determine the concentration [Mb] of photolyzed protein in the high concentration samples, we assume that the extinction coefficient changes upon CO photolysis are the same for both the low and high concentration samples. Then the photolyzed protein concentration for the high

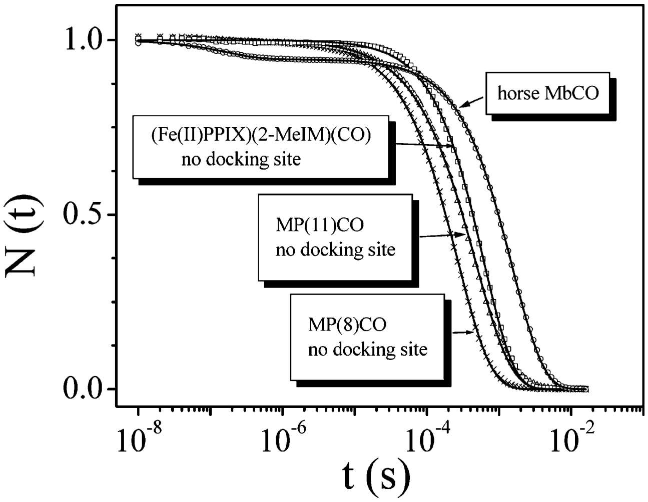

FIGURE 2: CO recombination upon flash photolysis at 293 K for horse heart Mb (○), MP(11) (△), MP(8) (×) and Fe(II)(PPIX)(2-MeIm) (□), detected at the Soret peak of each sample. Note the absence of geminate CO recombination in MP(11), MP(8), and Fe(II)(PPIX)(2-MeIm). These three samples were prepared at low concentration in the presence of CTAB to prevent aggregation.

concentration sample can be calculated from the absorbance changes, $[\mathrm{Mb}]_\mathrm{H} = [\mathrm{Mb}]_\mathrm{L}(\Delta A_\mathrm{H}/\Delta A_\mathrm{L})(l_\mathrm{L}/l_\mathrm{H})$, where $[\mathrm{Mb}]_\mathrm{L}$ is the photolyzed protein concentration for the low concentration sample, l_L and l_H are the optical path lengths for the low and high concentration samples, respectively. The $\Delta A_{\mathrm{L,H}}$ are the experimentally observed absorbance changes for low and high concentration samples at $t = 0$. This procedure leads to estimated uncertainties of 20% for $[\mathrm{Mb}]_\mathrm{H}$ and 19% for k_on, mainly due to uncertainties in the path length of the high concentration sample.

For low protein concentrations, $[\mathrm{Mb}] < 0.1$ mM $\ll$ [CO], the normalized absorption change, $N(t)$, in eq 2 and the CO concentration independent observed bimolecular rebinding rate k_on in eq 3 reduce to

$$N(t) = I_\mathrm{g} e^{-(k_\mathrm{g} t)^{\beta}} + (1 - I_\mathrm{g}) e^{-k_\mathrm{s} t}$$
$$k_\mathrm{on} = k_\mathrm{s}/[\mathrm{CO}] \tag{4}$$

In this case, $[\mathrm{CO}] \approx [\mathrm{CO}]_\mathrm{eq}$ and it is appropriate to set $[\mathrm{CO}]_\mathrm{eq}$ equal to the concentration of dissolved CO in water: 1.0 mM at 293 K and 1.56 mM at 273 K (*63*).

In summary, the experimental kinetics data for low concentration samples (<0.1 mM) are fitted using eq 4. For high protein concentrations, the CO concentration in the solvent cannot be treated as a constant during the rebinding process. For these samples, we use eq 2 to fit the experimental kinetics data.

RESULTS

Kinetics of Model Compounds. To evaluate the overall influence of the distal side protein residues on binding of a diatomic ligand, we study CO rebinding to MP and protoporphyrin IX complexed with 2-MeIm. The globular protein material of MP and Fe(II)(PPIX)(2-MeIm) has been partly or completely stripped off, but the proximal side of the iron is still bound with histidine (MP) or 2-methylimidazole [Fe(II)(PPIX)(2-MeIm)]. We use these samples to radically modify the distal side of the heme and thus evaluate the significance of a distal “docking site” (*26*, *27*) on the kinetics of diatomic ligand rebinding. Figure 2 shows CO recombination upon flash photolysis at 293 K for horse heart Mb, MP(11), MP(8), and Fe(II)(PPIX)(2-MeIm). Apparently, so long as the model compound samples are prepared at low concentration in CTAB micelles (to prevent aggregation), there is no CO geminate recombination in the nanosecond to millisecond region. The kinetic parameters of horse MbCO and the various CO model compounds obtained from fits using eq 4 are listed in Table 1.

Table 1: Rate Constants for CO Rebinding to Horse Mb, MP, and Model Compounds at 293 K[a]

	I_g (%)	k_g (10^6 s^{-1})	β	$1 - I_\mathrm{g}$ (%)	k_on (10^6 s^{-1} M^{-1})	β_1
horse MbCO	5.5	6.0	0.91	94	0.65	n.a
MP(11)CO	0	n.a.[b]	n.a	100	2.5	0.89
MP(8)CO	0	n.a	n.a	100	3.7	0.94
Fe(PPIX)(2-MeIm)(CO)	0	n.a	n.a	100	1.6	1.0

[a] The MbCO data are fit with eq 4, while the bimolecular phase for CO rebinding to MP(11) and MP(8) is slightly nonexponential. The actual fitting function for the CO-bound MP and model compound is $\Delta A = \Delta A_0 e^{-(k_\mathrm{s} t)^{\beta_1}}$, $0 \leq \beta_1 \leq 1$. [b] n.a. = not applicable.

Since there is no CO geminate recombination in MP and Fe(II)(PPIX)(2-MeIm), the kinetic data of these model compounds are fitted only by the bimolecular (second) term in eq 4. However, the bimolecular phase for MP(11) and MP(8) deviates slightly from a perfect exponential and the actual fitting function used is $\Delta A = \Delta A_0 e^{-(k_\mathrm{s} t)^{\beta_1}}$, with β_1 close to unity. Previous investigations of CO rebinding to aggregated MP(11) at 293 K (*52*, *64*) and in mixed solvents at 298 K (*52*, *65*) reported a bimolecular rate for CO rebinding $k_\mathrm{on} = 2 \times 10^7$ M^{-1} s^{-1}, one order of magnitude faster than the value 2.5×10^6 M^{-1} s^{-1} that we observe for monodisperse MP(11)CO in aqueous solution (Table 1). We also observed about one order of magnitude faster CO bimolecular rebinding in the CO complex of aggregated MP(11) at millimolar concentrations in the absence of CTAB (cf. Figure 4). The bimolecular CO binding rate observed for Fe(II)(PPIX)(2-MeIm) in CTAB ($k_\mathrm{on} = 1.6 \times 10^6$ s^{-1} M^{-1}) is in reasonable agreement with previous work on 2-MeIm ligated and 1-MeIm ligated mesoheme dimethyl ester in CTAB ($k_\mathrm{on} = 4.8 \times 10^5$ and 5.8×10^6 s^{-1} M^{-1}, respectively (*40*).

Clearly, an important issue for preparing aqueous MP and protoporphyrin IX samples is preventing molecular dimerization or aggregation (*52*, *56*, *66*−*68*), which takes place even for the CO complex (*69*). Efforts must be made to prevent sample aggregation because the intermolecular interactions due to dimerization or aggregation complicate the CO rebinding measurement. We use detergent (CTAB) and low sample concentrations (<0.1 mM) to prevent the samples from aggregating (*56*, *66*, *67*, *70*, *71*). Figure 3 shows examples of the absorption spectra of the high concentration (>1 mM) aggregated MP(11) samples (without CTAB) and the low concentration (<0.1 mM) nonaggregated MP(11) samples (with CTAB). The spectral differences are particularly pronounced for the ferrous form, where the presence of two distinct bands in the 500−600 nm range in the spectrum of the high concentration aggregated sample is characteristic of a six-coordinate low-spin heme. In contrast, the spectrum of the low concentration sample

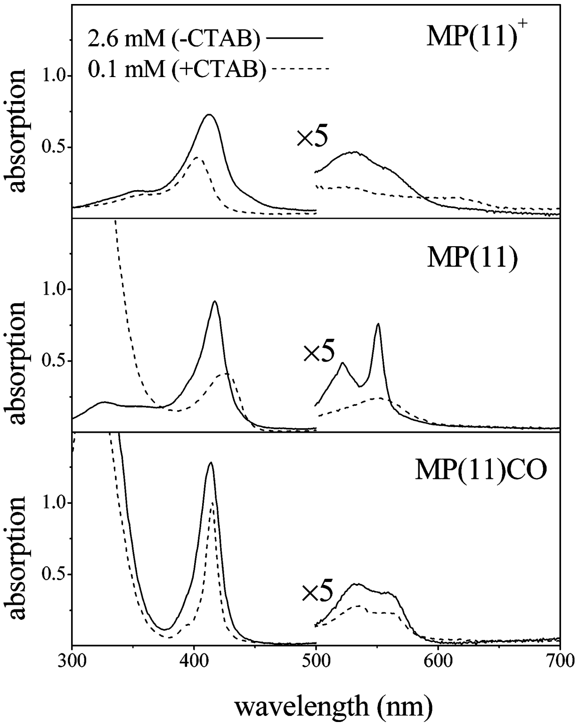

FIGURE 3: Spectroscopic signatures for aggregation of MP(11). The figure shows the absorption spectra for the aggregated (solid line, ∼2.6 mM, without CTAB, 50 μm path length) and nonaggregated (dashed line, ∼100 μM, with CTAB, 1-mm path length) MP(11) samples. In each case, the 500−700 nm region is expanded by a factor of 5. $MP(11)^+$ denotes ferric MP(11).

resembles that of deoxyMb, and is characteristic of a high-spin five-coordinate species. Spectral changes attributed to aggregation are also evident in the reduced CO-bound and oxidized forms at high concentration in the absence of detergent. The sixth axial ligand present in the high concentration deoxy form (the fifth being provided by the imidazole nitrogen of His18) is proposed to be the α-nitrogen of a valine or a lysine residue resulting from aggregation with another MP(11) molecule (*71*, *72*). It is noteworthy that the conversion from high-spin to low-spin spectra with increasing MP(11) concentration (Figure 3) is inconsistent with the assignment (*68*) of the low-spin spectrum to a monodisperse solution of MP(11) with water as a strong sixth ligand (i.e., water binding should not depend on MP(11) concentration).

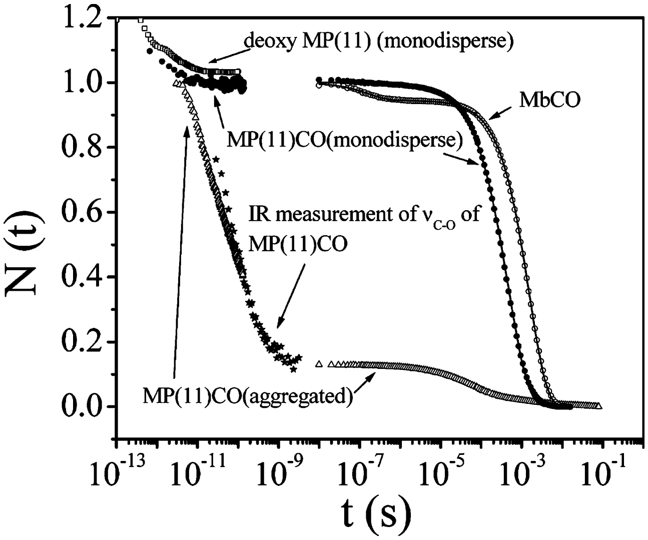

FIGURE 4: CO rebinding kinetics of aggregated and nonaggregated MP(11)CO samples. In the picosecond region, monodisperse MP(11) samples (50−100 μM in the presence of CTAB) were monitored at 415 nm with a bandwith of 0.5 nm. The MP(11)CO data was rescaled according to the average value around 100 ps and deoxy MP(11) was rescaled to compare with MP(11)CO. The ultrafast data for aggregated MP(11)CO (2.6 mM, no CTAB) was monitored at 425 nm with a bandwith of 0.5 nm and rescaled according to the value at 3 ps. In the nanosecond region, samples were measured at their Soret peaks, 423 nm for MbCO, 415 nm for monodisperse MP(11)CO. The aggregated MP(11)CO data in the nanosecond region was rescaled to match the aggregated MP(11)CO data in the picosecond region. The IR kinetic data of Lim et al (*29*) are plotted for comparison (sample concentration 10−20 mM, no CTAB). In the absence of aggregation, photolyzed MP(11)CO lacks the ∼100 ps geminate recombination previously attributed to removal of the distal pocket. In contrast, most CO rebinds geminately when aggregation occurs. On the basis of comparison of the ultrafast absorbance changes of MP(11)CO and deoxy MP(11), the 6-ps decay shown in the figure is assigned to vibrational cooling.

To probe the kinetic consequences of MP dimerization or "aggregation", we compare in Figure 4 the optical (Soret band) measurements of CO rebinding in "aggregated" and "nonaggregated" MP(11) samples. The infrared (IR) measurements of MP(11)CO by Lim et al. (*29*, *30*) (sample concentration 10−20 mM, without CTAB (*73*)), which use the IR intensity of the C−O stretching vibration as a measure of bound state population, are also shown. It can be seen that aggregation dramatically influences the observed CO geminate rebinding kinetics. The transient absorption signal from the low concentration, micelle-encapsulated MP(11) sample shows no geminate CO binding. The only ultrafast response in the transient spectra of MP(11)CO is a small ∼4−6 ps decay, which we attribute to a cooling process (*59*), rather than CO rebinding, since a similar signal is also seen in deoxy MP(11) (Figure 4). In contrast, when aggregation occurs at high concentration, most of the CO rebinds geminately with a time constant of about 100 ps. The kinetics of CO recombination measured at 425 nm in the aggregated sample matches the result reported previously in the IR measurements (*29*, *30*), where very high concentrations (10−20 mM (*73*)) are required to monitor the recovery of the IR C−O stretching band with acceptable signal-to-noise.

High protein concentration (>1 mM) might conceivably influence solvent properties, such as CO solubility and water activity. For example, the 32 nm^3 volume of hydrated Mb (*74*) accounts for 25% of the entire sample volume at the 13 mM concentration employed in transient IR measurements on MbCO (*73*). Moreover, the CO concentration in the solvent is no longer constant during CO rebinding. Consequently, we also investigated the effects of high protein concentrations on the CO rebinding kinetics of Mb, to help clarify interpretation of the IR measurements of MP(11) obtained at high concentration (*29*, *30*). Figure 5 compares CO rebinding kinetics to horse Mb at high (9.1 mM) and at low (96 μM) concentration. The data in Figure 5 were fitted using eq 2, and the results are listed in Table 2. Note that, in the high concentration sample, the bimolecular rebinding kinetics are primarily determined by the protein concentration [Mb], rather than by the free CO concentration $[CO]_{eq}$, which is reduced compared to the low concentration sample due to reduced CO solubility in the presence of high concentration protein. It is clear from Table 2 that both the geminate

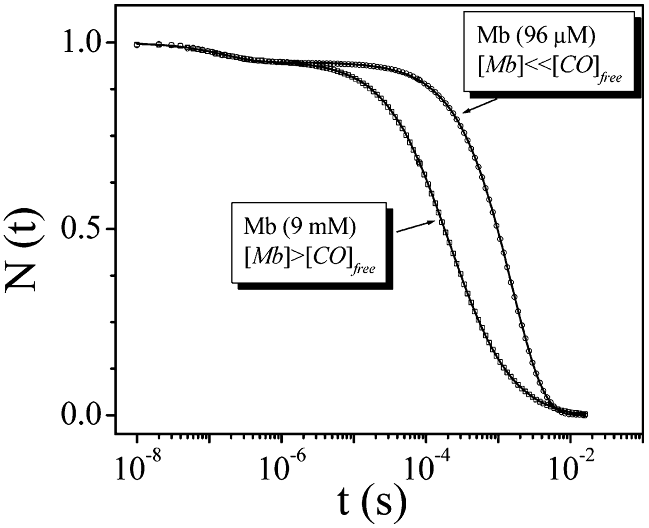

FIGURE 5: The CO rebinding kinetics of horse Mb in phosphate buffer pH 7 at room temperature.

Table 2: Protein Concentration Dependence of the CO Rebinding Kinetics in Horse Myoglobin at Room Temperature

sample conc	I_g (%)	k_g (10^6 s^{-1})	β	k_{on} (10^6 s^{-1} M^{-1})	[Mb] (mM)	[CO]$_{eq}$ (mM)
high	5.1	6.7	1	0.53	9.1	0.27
low	5.2	6.1	1	0.61	0.096	1

and bimolecular CO rebinding rate constants (k_g and k_{on}) of Mb are independent of the protein concentration within the experimental uncertainty. Thus, high transient CO concentrations following photolysis at high protein concentration are sufficient to explain the differences between the high and low concentration bimolecular processes shown in Figure 5. These results confirm that the concentration dependence of MP(11) (shown in Figure 4) reflects sample dimerization or aggregation, rather than effects due to time-dependent ligand (CO) concentration.

Resonance Raman Measurements of Microperoxidase. To probe aggregation-induced structural perturbations so that we could better understand the rapid CO geminate recombination, we measured cw and time-resolved resonance Raman spectra of MP(11) and MP(8). Figure 6 shows cw resonance Raman spectra of aggregated and nonaggregated deoxy MP(11) and MP(11) CO complexes. Figure 7 shows the 10-ns transient resonance Raman spectra of the aggregated and nonaggregated MP(11) CO complex. (In Figures 6 and 7 and throughout the text, we use the term "aggregated" to refer to samples with high sample concentration without CTAB and the term "nonaggregated" to refer to samples with low sample concentration in the presence of CTAB.)

In traces b and c of Figure 6, the ν_3 doublet in the spectra of the high concentration (aggregated) deoxy MP(11) and the CO dissociated form suggests a mixture of high-spin and low-spin species. The upshifted ν_2 (~1590 cm^{-1}) relative to the low concentration (nonaggregated) sample (~1573 cm^{-1}), along with the ratio of the intensities of the high-spin and low-spin ν_3 bands, indicate that the high concentration sample is predominantly low-spin. This suggests that dimerization or aggregation takes place between MP(11) molecules in the high concentration samples. There is no sign of an Fe−N$_{His}$ stretching mode in the high concentration (aggregated) deoxy MP(11) sample or in its CO photoproduct (Figure 6).

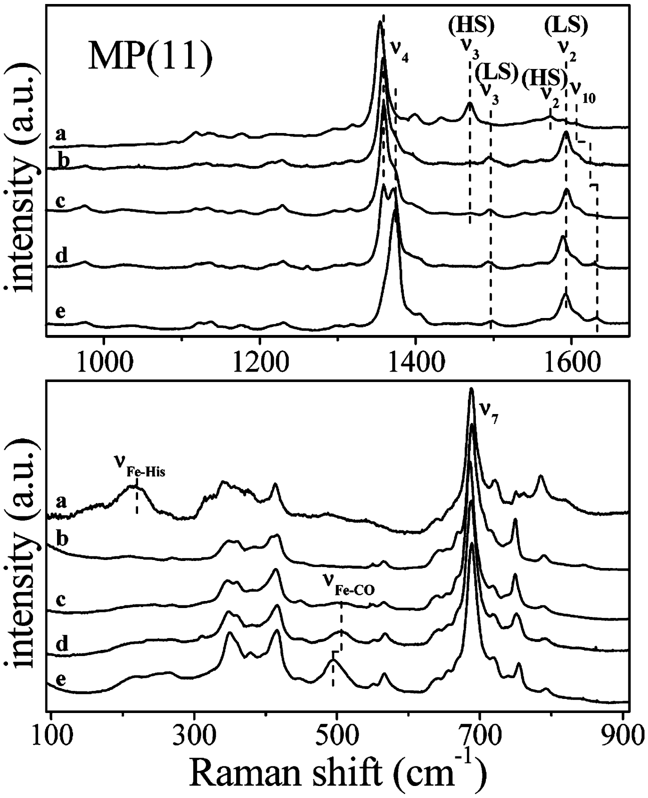

FIGURE 6: The cw resonance Raman spectra of deoxy MP(11) and MP(11) CO complexes: (a) deoxy (no aggregation), spherical focusing lens, static cell, 17 mW; (b) deoxy (aggregated), spherical focusing lens, static cell, 17 mW; (c) CO photolyzed (aggregated), spherical focusing lens, static cell, 47 mW; (d) CO partially photolyzed (aggregated), cylindrical focusing lens, static cell, 5 mW; and (e) CO-bound (aggregated), cylindrical focusing lens, spinning cell, 17 mW. The sample concentrations are ~2 mM without CTAB for the aggregated samples and ~100 μM with CTAB for nonaggregated samples. The doublet of ν_3 bands in the Raman spectra of the high concentration (aggregated) deoxy MP(11) (b) and CO dissociated MP(11) (c) indicates mixture of high-spin and low-spin species. There is no sign of the ~220 cm^{-1} Fe−N$_{His}$ stretching mode in the high concentration (aggregated) deoxy MP(11) (b) and CO photolyzed MP(11) (c). The asymmetric Fe−CO stretching band of the high concentration (aggregated) MP(11)CO (e) and the upshift of the Fe−CO stretching band in the CO partially photolyzed MP(11) sample (d) suggest that two overlapping Fe−CO stretching modes are present.

For the high concentration (aggregated) samples, the Fe−CO stretching mode in the partially dissociated MP(11)CO (trace d in Figure 6) is upshifted about 10 cm^{-1} compared to the Fe−CO stretching mode (495 cm^{-1}) of the fully ligated sample (trace e in Figure 6). The asymmetric Fe−CO stretching band (trace e in Figure 6) and its upshift in the partially photolyzed sample (trace d in Figure 6) suggest overlapping contributions from more than one Fe−CO stretching mode in the high concentration (aggregated) MP(11)CO samples. The higher frequency Fe−CO vibration (~505 cm^{-1}) is difficult to photolyze and may relate to the very fast CO geminate rebinding observed in the aggregated MP samples. We previously observed changes in the relative intensity of two Fe−CO bands in partially unfolded MbCO at low pH under continuous illumination (*34*), which we modeled as a photostationary equilibrium between differing

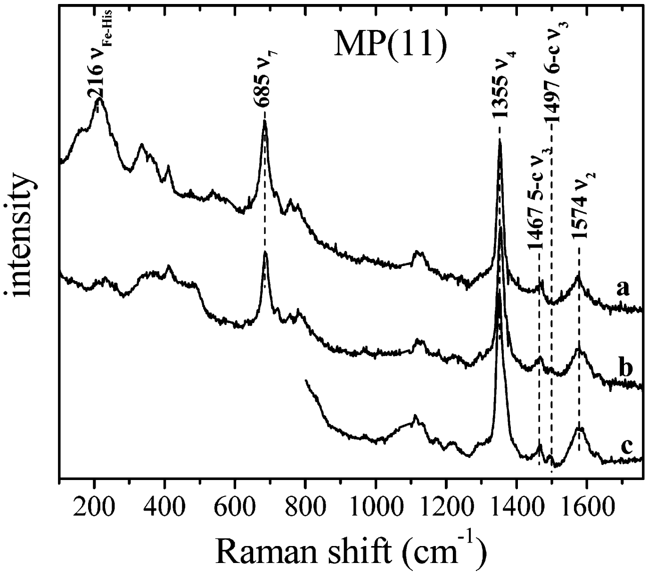

FIGURE 7: The 10-ns transient resonance Raman spectra of MP(11) CO complex: (a) MP(11)CO (no aggregation), (b) MP(11)-CO (aggregated), and (c) (MP(11)CO (aggregated) in spinning cell. The excitation pulse energy is about 100 μJ. The sample concentrations are similar to the sample concentrations in Figure 6 for the aggregated and nonaggregated samples. The third spectrum (c) shows the high-frequency region of MP(11)CO as a control measurement (b and c are the same). The single ν_4 band at 1355 cm^{-1} in all Raman spectra indicates CO has been totally dissociated. The core size marker bands (ν_3 and ν_2) suggest that most of the sample is five-coordinate high-spin species in the high concentration (aggregated) samples (b and c). However, there is still no Fe−N$_{His}$ stretching mode in these samples. There is a broad quartz band underneath the spectrum (b) in the 300−500 cm^{-1} region (trace b) due to the wall of quartz sample cell. This occurs when the laser is positioned near the sample surface to avoid strong self-absorption in high concentration samples.

proximal ligands. Similar proximal ligand switch models have been proposed for model heme compounds and the Mb H93G mutant (*35*, *37*) and may be operative in these aggregated model systems as well.

The Fe−CO stretching band for low concentration (nonaggregated) MP(11)CO is at 491 cm^{-1} and also asymmetric (*76*). However, in contrast to the high concentration (aggregated) MP(11)CO, the Raman spectra of the partially photolyzed low concentration (nonaggregated) MP(11)CO show that the Fe−CO stretching band has reduced intensity, but is not shifted (*76*). The Raman spectrum of the low concentration (nonaggregated) deoxy MP(11) (trace a in Figure 6) shows a strong Fe−N$_{His}$ band at 218 cm^{-1} and the core size marker bands ν_4, ν_3, and ν_2 indicate that the nonaggregated deoxy MP(11) is a five-coordinate high-spin sample. The cw Raman shifts of the MP(11) samples in Figure 6, along with the low concentration (nonaggregated) MP(11)CO sample, are summarized in Table 3. These Raman shifts agree well with previous Raman measurements of aggregated and nonaggregated deoxy MP(8) samples (*70*). The Raman shifts of the deoxy and CO complexes of MP(11) listed in Table 3 do not agree with the measurements of Laberge et al. (*68*).

For all 10-ns transient Raman spectra of MP(11)CO in Figure 7, the presence of a single ν_4 band at 1355 cm^{-1} indicates that CO is completely dissociated. The core size marker bands ν_3 and ν_2 suggest that most of the photoproduct is a five-coordinate high-spin species, even for the aggregated samples in Figure 7. Nevertheless, there is still no Fe−N$_{His}$ stretching mode observed in the 10-ns transient spectra of the aggregated samples. The very similar Raman spectra for the aggregated MP(11)CO using both a static and spinning cell (trace b and c in Figure 7) confirm that the 10-ns Raman spectra represent the photoproduct of the aggregated MP(11)CO sample. The 10-ns transient Raman spectrum of the nonaggregated MP(11)CO in Figure 7 (trace a) is very similar to the cw Raman spectrum of the nonaggregated deoxy MP(11) in Figure 6 (trace a). This is consistent with previous work on Mb (*75*) and means that five-coordinate high-spin deoxy MP(11) is the transient photoproduct in the low concentration (nonaggregated) MP(11)CO samples. One significant difference between the high concentration (aggregated) MP(11)CO cw Raman spectra in Figure 6 and the transient Raman spectra in Figure 7 is the different ratio of high and low spin species. The 10-ns transient photoproduct of the aggregated MP(11)CO sample is primarily five-coordinate high spin (traces b and c in Figure 7) with no Fe−His mode, while the long time transient photoproduct probed by the cw Raman experiment is primarily a low-spin species after CO photolysis (trace c in Figure 6). This indicates that on time scales much longer than 10 ns, another Fe ligand replaces the photolyzed CO in the aggregated samples.

The 10-ns transient resonance Raman spectra of MP(8)-CO at high and low concentration are shown in Figure 8. "Nonaggregated" MP(8)CO (trace a in Figure 8) can be studied at low concentration without CTAB, since the aggregation of MP(8) is less severe than for MP(11). The strong Fe−N$_{His}$ mode and core size marker bands indicate that the photoproduct of the "nonaggregated" MP(8)CO sample is a five-coordinate, histidine ligated high-spin species. The ultrafast kinetics measurements of CO rebinding to low concentration MP(8) without CTAB also show no picosecond geminate CO rebinding (*76*). This observation is consistent with the concept that the picosecond CO geminate rebinding somehow arises from the sample aggregation process. Similarly, the transient Raman spectrum of aggregated MP(8) shows no Fe−N$_{His}$ stretching mode following CO photodissociation (trace b in Figure 8) even though the core size marker bands indicate that the dominant species is five-coordinate high-spin. This appears to be correlated with the observation of picosecond CO geminate rebinding (*76*).

The transient Raman spectra of MP(8)CO in Figure 8 are very similar to those of MP(11)CO shown in Figure 7. They are also in good agreement with the previously reported Raman measurements of deoxy MP(8) (*70*). However, the Fe−N$_{His}$ stretching mode in the (nonaggregated) MP(8)CO photoproduct is upshifted to 225 cm^{-1} (trace a in Figure 8) compared to ∼216 cm^{-1} for nonaggregated deoxy MP(11) (trace a in Figure 6) and its CO photoproduct (trace a in Figure 7). By studying the CTAB dependence of the Fe−N(2-MeIm) stretching band in the nonaggregated five-coordinate high-spin Fe(PPIX)(2-MeIm) samples, Kitagawa's group (*77*, *78*) concluded that the upshifted Fe−N(2-MeIm) mode (220 cm^{-1} (*79*) in the absence of CTAB compared to 207 cm^{-1} (*80*) in the presence of CTAB) is due to the hydrogen bonding between the heme proximal 2-MeIm and solvent water. Similar effects could conceivably be involved

Table 3: Raman Shifts of MP(11) Complex Measured by cw Laser Line Excitation

sample	$\nu_{\mathrm{Fe-His}}$ (cm^{-1})	$\nu_{\mathrm{Fe-CO}}$ (cm^{-1})	ν_7 (cm^{-1})	ν_4 (cm^{-1})	ν_3 (cm^{-1})	ν_2 (cm^{-1})	ν_{10} (cm^{-1})
deoxy (HS) (monodisperse)	218	n.a.	688	1354	1470	1573	1605
deoxy (LS) (aggregation)	n.d.[a]	n.a.	688	1358	1473(HS) 1494(LS)	1593	1621
CO photolyzed (aggregation)	n.d.	n.a.	686	1359	1470(HS) 1495(LS)	1594	n.d.
CO bound (aggregation)	n.d.	495 505	688	1374	1498	1592	1631
CO bound (monodisperse)	n.d.	491	689	1372	1499	1591	n.d.

[a] n.d. = not determined. n.a. = not applicable.

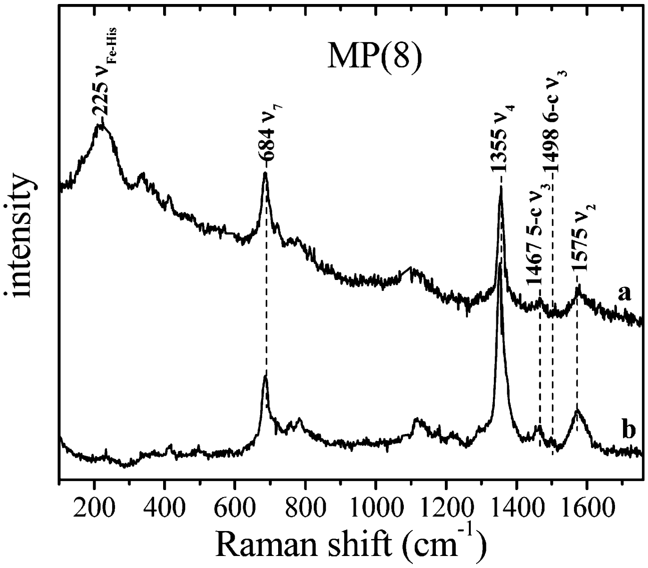

FIGURE 8: The 10-ns transient resonance Raman spectra of MP(8)CO: (a) without aggregation (50 μM, without CTAB) and (b) with aggregation (3 mM, without CTAB). The excitation pulse energy is about 100 μJ. There is no Fe−N$_{\mathrm{His}}$ stretching mode in the CO dissociated aggregated MP(8) sample (b) even though the core size marker bands indicate that most of the hemes are five-coordinate high-spin.

in upshifting the Fe−N$_{\mathrm{His}}$ transient Raman band in the nonaggregated MP(8) samples.

DISCUSSION

Ultrafast optical measurements of CO-bound MP(11) (Figure 4), MP(8) (*76*), and Fe(II)(PPIX)(2-MeIm) (*81*), all of which lack an organized distal pocket structure, provide no evidence for rapid geminate CO rebinding when the monomer forms are studied. The results in Figure 2 and Table 1 demonstrate that the elimination of the distal heme pocket (and more specifically, the protein residues proposed to form a ligand "docking site" (*26*, *27*) in Mb) do not influence geminate CO rebinding as dramatically as previously claimed (*29*, *30*). The prior conclusions were based upon IR measurements using highly concentrated (and aggregated) samples, which lead to anomalous CO rebinding kinetics.

The results presented here are completely consistent with a previous report (*53*) that there is no observable CO rebinding to imidazole-ligated protoheme complexes on picosecond time scales in low viscosity solvents. It is worth noting that analogous measurements of CO rebinding kinetics in organic solvents and in aqueous CTAB preparations agree well, suggesting that the use of either solvent condition will generate self-consistent results (*40*). Similarly, no significant geminate CO recombination was observed for Fe(PPIX)(His)(CO) in 80% ethylene glycol solutions (*35*), although at extreme viscosity (98% glycerol), CO geminate rebinding was observed (*53*).

These results, combined with the present kinetic results on CO rebinding to MP and Fe(II)(PPIX)(2-MeIm), suggest that, in low viscosity solvents, the CO escape rate k_{out} in eq 1 is much larger than the CO geminate binding rate k_{BA}, i.e., $k_{\mathrm{out}} \gg k_{\mathrm{BA}}$. This means that, within the three-state model described in eq 1, the geminate yield $k_{\mathrm{BA}}/(k_{\mathrm{BA}} + k_{\mathrm{out}})$ is negligible and k_{BA} cannot be obtained.

In contrast, the significant CO geminate rebinding that is observed following photolysis of Fe(II)(PPIX)(1-MeIm)(CO) in 98% glycerol (*53*) demonstrates that when the CO escape rate k_{out} is slowed by highly viscous solvents or distal protein residues, the geminate yield is increased to an observable level.

It is clear that the distal pocket significantly influences the kinetics of ligand rebinding. Numerous prior studies of heme proteins (*3*, *5*−*11*, *14*−*17*, *82*) have shown that the rebinding kinetics are dependent on the polarity and size of individual residues in the distal pocket. However, what we want to emphasize here is that the elimination of the putative "docking site" in the distal pocket of Mb does not result in the 10^5-fold increase in the geminate binding rate proposed by Lim et al (*29*, *30*).

On the other hand, the data in Figure 4 do confirm the observation of a large amplitude ∼100 ps CO geminate rebinding process for MP(11) when a high concentration (aggregated) sample is used. Our extensive rebinding, cw Raman, and transient Raman studies of these high concentration (aggregated) MP samples suggest that the fast CO geminate rebinding is associated with proximal perturbations of the aggregated molecules. The different ratio of high-spin and low-spin species detected in the cw and transient Raman spectra of the high concentration (aggregated) MP photoproduct (Figures 6−8), combined with kinetic studies, suggests the scheme

$$\mathrm{L{-}Fe{-}CO} \xrightleftharpoons{h\nu} \mathrm{L{-}Fe} \xrightleftharpoons{\sim 1\ \mathrm{ms}} \mathrm{L{-}Fe{-}L'} \qquad (5)$$

for CO photolysis in the aggregated MP(11) and MP(8) samples, where L is the proximal ligand of the heme iron. When a high cw flux of photons drives CO from the heme iron, a different ligand L′ (perhaps the α-nitrogen of a valine or a lysine from another MP molecule (*71*, *72*)) can bind to the distal coordination site of the heme iron on millisecond time scales. Thus, continuous illumination in cw Raman measurements creates a photostationary equilibrium dominated by the L−Fe−L′ state. To account for the observation of multiple Fe−CO bands with differing behavior under photolysis, the simple reaction scheme in eq 5 could be expanded to include CO-ligated states with alternate proximal ligands. In contrast, the 10-ns transient Raman spectra measure the CO photodissociated L−Fe state denoted in eq 5.

Assuming that the 10-ns transient Raman spectra shown in Figures 7 and 8 reflect the initial photoproducts L−Fe of the aggregated MP(11) and MP(8) samples, the absence of an Fe−N_{His} mode in these spectra suggests three straightforward possibilities: (i) L is not the histidine residue, (ii) there is no proximal ligand (L) present, or (iii) intermolecular interactions keep the heme iron in plane following CO dissociation. In cases (i) and (ii), there is no Fe−N_{His} mode to detect. In the latter case (iii), the Raman Franck−Condon coupling to the resonant Soret band may be too small to allow detection of the Fe−N_{His} mode (*83*). All of these possibilities are consistent with fast CO geminate rebinding. However, infrared studies of the highly concentrated (aggregated) CO-bound MP(11) samples find a CO vibrational frequency of 1952 cm^{-1} (*76*). This, along with the observation of the 505 cm^{-1} Fe−CO Raman mode, is in agreement with the well-established back-bonding correlation between ν(Fe−CO) and ν(C−O) in ferrous histidine bound FeCO adducts (*84*−*86*). This observation suggests that proximal histidine ligation in a planar heme geometry (possibility (iii)) is most consistent with the experimental results. However, the question of the spin state of the iron atom in a five-coordinate in-plane geometry remains open and is potentially inconsistent with the Raman marker bands, which indicate a $S = 2$ state under these conditions. Therefore, a more complex scenario, involving a rapid proximal ligand switch mechanism (*34*, *35*, *37*), may ultimately need to be invoked to consistently explain all of the experimental observations and simultaneously account for the geminate rebinding of CO to the heme on the 100 ps time scale.

CONCLUSION

Our study finds no observable CO geminate rebinding in monodisperse MP or Fe(II)(PPIX)(2-MeIm) samples where the distal pocket has been removed. At high concentrations of MP(11)CO, when aggregation occurs, we observe that most of the CO rebinds geminately in about 100 ps, which is in agreement with previous infrared studies (*29*, *30*). However, contrary to previous suggestions (*29*, *30*), the kinetics and cw and transient Raman studies presented here demonstrate that this rapid geminate rebinding arises from perturbations of the proximal heme-ligand structure, rather than from the absence of a distal pocket “docking site”. The proximal perturbations do not allow detection of the Fe−His Raman mode and are potentially due to a planar, (rather than a domed) histidine ligated heme (*83*) or to a loss of the distal histidine ligand following CO dissociation (*35*). Either of these scenarios would enhance the CO geminate rebinding rate. We conclude that the IR rebinding studies of Lim et al. (*29*, *30*) do not imply that distal pocket docking effects are of primary importance in controlling CO rebinding. This is because the IR studies must be carried out at high sample concentrations and cannot distinguish distal pocket docking effects from other molecular dimerization or aggregation-induced phenomena that affect the proximal ligation.

The absence of the iron-proximal ligand stretching mode in the transient Raman photoproduct is an unambiguous signature of the proximal perturbations, which are clearly correlated with fast CO geminate rebinding in both the MP-(8) and MP(11) samples. Thus, the very fast CO geminate rebinding that is observed in both of the high concentration (aggregated) MP(8) and MP(11) samples strongly suggests that proximal perturbations play a significant role in controlling the geminate ligand rebinding rate. Finally, the lack of similar concentration-induced effects in native Mb verifies that studies of Mb under dilute conditions are applicable to the more concentrated regime found in the cellular milieu.

REFERENCES

1. Antonini, E., and Brunori, M. (1971) *Hemoglobin and Myoglobin in Their Reactions with Ligands*, North-Holland Publishing Co., Amsterdam-London.
2. Sage, J. T., and Champion, P. M. (1996) Small Substrate Recognition in Heme Proteins, in *Comprehensive Supramolecular Chemistry* (Suslick, K. S., Ed.) pp 171−218, Pergamon, Oxford, U. K.
3. Olson, J. S., and Phillips, G. N., Jr. (1996) Kinetic pathways and barriers for ligand binding to myoglobin, *J. Biol. Chem. 271*, 17593−17596.
4. Sage, J. T. (2004) Hemoglobins: O_2 Uptake and Transport, in *Encyclopedia of Supramolecular Chemistry*, Marcel Dekker, Inc., New York
5. Elber, R., and Karplus, M. (1990) Enhanced Sampling in Molecular Dynamics: Use of the Time-Dependent Hartree Approximation for a Simulation of Carbon Monoxide Diffusion through Myoglobin, *J. Am. Chem. Soc. 112*, 9161−9175.
6. Chu, K., Vojtěchovský, J., McMahon, B. H., Sweet, R. M., Berendzen, J., and Schlichting, I. (2000) Structure of a ligand-binding intermediate in wild-type carbonmonoxy myoglobin, *Nature 403*, 921−923.
7. Brunori, M. (2000) Structural dynamics of myoglobin, *Biophys. Chem. 86*, 221−230.
8. Brunori, M., Vallone, B., Cutruzzolà, F., Travaglini-Allocatelli, C., Berendzen, J., Chu, K., Sweet, R. M., and Schlichting, I. (2000) The role of cavities in protein dynamics: crystal structure of a photolytic intermediate of a mutant myoglobin, *Proc. Natl. Acad. Sci. U.S.A. 97*, 2058−2063.
9. Ostermann, A., Waschipky, R., Parak, F. G., and Nienhaus, G. U. (2000) Ligand binding and conformational motions in myoglobin, *Nature 404*, 205−208.
10. Scott, E. E., and Gibson, Q. H. (1997) Ligand migration in sperm whale myoglobin, *Biochemistry 36*, 11909−11917.
11. Scott, E. E., Gibson, Q. H., and Olson, J. R. (2001) Mapping the Pathways for O_2 Entry into and Exit from Myoglobin, *J. Biol. Chem. 276*, 5177−5188.
12. Sigfridsson, E., and Ryde, U. (2002) Theoretical study of the discrimination between O_2 and CO by myoglobin, *J. Inorg. Biochem. 91*, 101−115.
13. Spiro, T. G., and Kozlowski, P. M. (2001) Is the CO adduct of myoglobin bent, and does it matter? *Acc. Chem. Res. 34*, 137−144.
14. Olson, J. S., Mathews, A. J., Rohlfs, R. J., Springer, B. A., Egeberg, K. D., Sligar, S. G., Tame, J., Renaud, J. P., and Nagai, K. (1988) The role of the distal histidine in myoglobin and haemoglobin, *Nature 336*, 265−266.
15. Olson, J. S., and Phillips, G. N. (1997) Myoglobin discriminates between O_2, NO, and CO by electrostatic interactions with the bound ligand, *J. Biol. Inorg. Chem. 2*, 544−552.
16. Quillin, M. L., Arduini, R. M., Olson, J. S., and Phillips, G. N., Jr. (1993) High-resolution crystal structures of distal histidine mutants of sperm whale myoglobin, *J. Mol. Biol. 234*, 140−155.
17. Phillips, S. E. V. (1980) Structure and refinement of oxymyoglobin at 1.6 Å resolution, *J. Mol. Biol. 142*, 531−554.
18. Unno, M., Christian, J. F., Olson, J. S., Sage, J. T., and Champion, P. M. (1998) Evidence for Hydrogen Bonding Effects in the Iron Ligand Vibrations of Carbonmonoxy Myoglobin, *J. Am. Chem. Soc. 120*, 2670−2671.
19. Perutz, M. F., and Mathews, F. S. (1966) An X-ray study of azide methaemoglobin, *J. Mol. Biol. 21*, 199−202.

20. Chance, B., Ravilly, A., and Rumen, N. (1966) Reaction kinetics of a crystalline hemoprotein: an effect of crystal structure on reactivity of ferrimyoglobin, *J. Mol. Biol. 17*, 525−534.
21. Ringe, D., Petsko, G. A., Kerr, D. E., and Ortiz de Montellano, P. R. (1984) Reaction of myoglobin with phenylhydrazine: a molecular doorstop, *Biochemistry 23*, 2−4.
22. Zhu, L., Sage, J. T., Rigos, A. A., Morikis, D., and Champion, P. M. (1992) Conformational interconversion in protein crystals, *J. Mol. Biol. 224*, 207−215.
23. Yang, F., and Phillips, G. N., Jr. (1996) Crystal structures of CO-, deoxy- and met-myoglobins at various pH values, *J. Mol. Biol. 256*, 762−774.
24. Tian, W. D., Sage, J. T., Champion, P. M., Chien, E., and Sligar, S. G. (1996) Probing heme protein conformational equilibration rates with kinetic selection, *Biochemistry 35*, 3487−3502.
25. Cao, W., Christian, J. F., Champion, P. M., Rosca, F., and Sage, J. T. (2001) Water Penetration and Binding to Ferric Myoglobin, *Biochemistry 40*, 5728−5737.
26. Lim, M., Jackson, T. A., and Anfinrud, P. A. (1997) Ultrafast rotation and trapping of carbon monoxide dissociated from myoglobin, *Nat. Struct. Biol. 4*, 209−214.
27. Lim, M., Jackson, T. A., and Anfinrud, P. A. (1995) Mid-infrared vibrational-spectrum of CO after photodissociation from heme: Evidence for a ligand docking site in the heme pocket of hemoglobin and myoglobin, *J. Chem. Phys. 102*, 4355−4366.
28. Lim, M., Jackson, T. A., and Anfinrud, P. A. (1995) Binding of CO to myoglobin from a heme pocket docking site to form nearly linear Fe−C−O, *Science 269*, 962−966.
29. Lim, M., Jackson, T. A., and Anfinrud, P. A. (1997) Modulating carbon monoxide binding affinity and kinetics in myoglobin: the roles of the distal histidine and the heme pocket docking site, *J. Biol. Inorg. Chem. 2*, 531−536.
30. Lim, M., Jackson, T. A., and Anfinrud, P. A. (2001) Time-Resolved Infrared Studies of Ligand Dynamics in Heme Proteins, in *Ultrafast Infrared and Raman Spectroscopy* (Fayer, M. D., Ed.) pp 191−226, Marcel Dekker, Inc., New York.
31. Perutz, M. F. (1970) Stereochemistry of cooperative effects in haemoglobin, *Nature 228*, 726−739.
32. Barrick, D., Ho, N. T., Simplaceanu, V., Dahlquist, F. W., and Ho, C. (1997) A test of the role of the proximal histidines in the Perutz model for cooperativity in haemoglobin, *Nat. Struct. Biol. 4*, 78−83.
33. Šrajer, V., Reinisch, L., and Champion, P. M. (1988) Protein fluctuations, distributed coupling, and the binding of ligands to heme-proteins, *J. Am. Chem. Soc. 110*, 6656−6670.
34. Sage, J. T., Li, P. S., and Champion, P. M. (1991) Spectroscopic studies of myoglobin at low pH: heme ligation kinetics, *Biochemistry 30*, 1237−1247.
35. Huang, Y., Marden, M. C., Lambry, J. C., Fontaineaupart, M. P., Pansu, R., Martin, J. L., and Poyart, C. (1991) Photolysis of the histidine-heme-CO complex, *J. Am. Chem. Soc. 113*, 9141−9144.
36. Duprat, A. F., Traylor, T. G., Wu, G. Z., Coletta, M., Sharma, V. S., Walda, K. N., and Magde, D. (1995) Myoglobin NO at low pH: free 4-coordinated heme in the protein pocket, *Biochemistry 34*, 2634−2644.
37. Franzen, S., Bailey, J., Dyer, R. B., Woodruff, W. H., Hu, R. B., Thomas, M. R., and Boxer, S. G. (2001) A photolysis-triggered heme ligand switch in H93G myoglobin, *Biochemistry 40*, 5299−5305.
38. Chang, C. K., and Traylor, T. G. (1973) Proximal base influence on the binding of oxygen and carbon monoxide to heme, *J. Am. Chem. Soc. 95*, 8477−8479.
39. Geibel, J., Cannon, J., Campbell, D., and Traylor, T. G. (1978) Model compounds for R-state and T-state hemoglobins, *J. Am. Chem. Soc. 100*, 3575−3585.
40. White, D. K., Cannon, J. B., and Traylor, T. G. (1979) A Kinetic Model for R- and T-State Hemoglobin. Flash Photolysis of Heme-Imidazole-Carbon Monoxide Mixtures, *J. Am. Chem. Soc. 101*, 2443−2454.
41. Traylor, T. G. (1981) Synthetic Model Compounds for Hemoproteins, *Acc. Chem. Res. 14*, 102−109.
42. Traylor, T. G., Taube, D. J., Jongeward, K. A., and Magde, D. (1990) Steric effects on geminate recombinations, *J. Am. Chem. Soc. 112*, 6875−6880.
43. Cao, W., Sjodin, T., Sage, J. T., Ye, X., Demidov, A. A., Wang, W., Champion, P. M., and Barrick, D. (2001) Proximal and Distal Influences on Ligand Binding to Heme Proteins, *Biophys. J. 80*, 283a.
44. Carver, T. E., Rohlfs, R. J., Olson, J. S., Gibson, Q. H., Blackmore, R. S., Springer, B. A., and Sligar, S. G. (1990) Analysis of the kinetic barriers for ligand-binding to sperm whale myoglobin using site-directed mutagenesis and laser photolysis techniques, *J. Biol. Chem. 265*, 20007−20020.
45. Harvey, J. N. (2000) DFT Computation of the Intrinsic Barrier to CO Geminate Recombination with Heme Compounds, *J. Am. Chem. Soc. 122*, 12401−12402.
46. McMahon, B. H., Stojkovic, B. P., Hay, P. J., Martin, R. L., and Garcia, A. E. (2000) Microscopic model of carbon monoxide binding to myoglobin, *J. Chem. Phys. 113*, 6831−6850.
47. Kumazaki, S., Nakajima, H., Sakaguchi, T., Nakagawa, E., Shinohara, H., Yoshihara, K., and Aono, S. (2000) Dissociation and recombination between ligands and heme in a CO-sensing transcriptional activator CooA. A flash photolysis study, *J. Biol. Chem. 275*, 38378−38383.
48. Kundu, S., Snyder, B., Das, K., Chowdhury, P., Park, J., Petrich, J. W., and Hargrove, M. S. (2002) The leghemoglobin proximal heme pocket directs oxygen dissociation and stabilizes bound heme, *Proteins 46*, 268−277.
49. Miers, J. B., Postlewaite, J. C., Cowen, B. R., Roemig, G. R., Lee, I. Y. S., and Dlott, D. D. (1991) Preexponential-limited solid-state chemistry: ultrafast rebinding of a heme ligand complex in a glass or protein matrix, *J. Chem. Phys. 94*, 1825−1836.
50. Austin, R. H., Beeson, K. W., Eisenstein, L., Frauenfelder, H., and Gunsalus, I. C. (1975) Dynamics of ligand binding to myoglobin, *Biochemistry 14*, 5355−5373.
51. Negrerie, M., Bouzhir, L., Martin, J. L., and Liebl, U. (2001) Control of nitric oxide dynamics by guanylate cyclase in its activated state, *J. Biol. Chem. 276*, 46815−46821.
52. Adams, P. A., Baldwin, D. A., and Marques, H. M. (1996) The Hemepeptides from Cytochrome *c*: Preparation, Physical and Chemical Properties, and Their Use as Model Compounds for the Hemoproteins, in *Cytochrome C. A Multidisciplinary Approach* (Scott, R. A., and Mauk, A. G., Eds.) pp 635−692, University Science Books, Sausalito, California, USA.
53. Traylor, T. G., Magde, D., Taube, D. J., Jongeward, K. A., Bandyopadhyay, D., Luo, J. K., and Walda, K. N. (1992) Geminate recombination of carbon-monoxide complexes of hemes and heme-proteins, *J. Am. Chem. Soc. 114*, 417−429.
54. Sage, J. T., Morikis, D., and Champion, P. M. (1991) Spectroscopic studies of myoglobin at low pH: heme structure and ligation, *Biochemistry 30*, 1227−1237.
55. Salmeen, I., Rimai, L., and Babcock, G. T. (1978) Raman spectra of heme a, cytochrome oxidase-ligand complexes, and alkaline denatured oxidase, *Biochemistry 17*, 800−806.
56. Carraway, A. D., Povlock, S. L., Houston, M. L., Johnston, D. S., and Peterson, J. (1995) Monomeric ferric heme peptide derivatives: model systems for hemoproteins, *J. Inorg. Biochem. 60*, 267−276.
57. Wang, W., Ye, X., Demidov, A. A., Rosca, F., Sjodin, T., Cao, W., Sheeran, M., and Champion, P. M. (2000) Femtosecond Multi-Color Pump−Probe Spectroscopy of Ferrous Cytochrome *c*, *J. Phys. Chem. B 104*, 10789−10801.
58. Ye, X., Demidov, A. A., and Champion, P. M. (2002) Photodissociation quantum yield of MbNO, MbO2 and heme vibrational relaxation, *J. Am. Chem. Soc. 124*, 5914−5924.
59. Ye, X., Demidov, A., Rosca, F., Wang, W., Kumar, A., Ionascu, D., Zhu, L., Barrick, D., Wharton, D., and Champion, P. M. (2003) Investigations of heme protein absorption lineshapes, vibrational relaxation, and resonance Raman scattering on ultrafast timescales, *J. Phys. Chem. A 107*, 8156−8165.
60. Christian, J. F., Unno, M., Sage, J. T., Champion, P. M., Chien, E., and Sligar, S. G. (1997) Spectroscopic effects of polarity and hydration in the distal heme pocket of deoxymyoglobin, *Biochemistry 36*, 11198−11204.
61. Peterson, E. S., and Friedman, J. M. (1998) A possible allosteric communication pathway identified through a resonance Raman study of four beta 37 mutants of human hemoglobin A, *Biochemistry 37*, 4346−4357.
62. Henry, E. R., Sommer, J. H., Hofrichter, J., and Eaton, W. A. (1983) Geminate recombination of carbon-monoxide to myoglobin, *J. Mol. Biol. 166*, 443−451.
63. Seidell, A. (1940) *Solubilities of Inorganic and Metal Organic Compounds; A Compilation of Quantitative Solubility Data from the Periodical Literature*, D. Van Nostrand Company, Inc., New York.
64. Sharma, V. S., Ranney, H. M., Geibel, J. F., and Traylor, T. G. (1975) A new method for the determination of ligand dissociation

rate constant of carboxyhemoglobin, *Biochem. Biophys. Res. Commun. 66*, 1301−1306.

65. Hasinoff, B. B. (1981) Diffusion-controlled reaction kinetics of the binding of carbon monoxide to the heme undecapeptide of cytochrome *c* (microperoxidase 11) in high viscosity solvents, *Arch. Biochem. Biophys. 211*, 396−402.
66. Urry, D. W. (1967) Model systems for interacting heme moieties. I. The heme undecapeptide of cytochrome *c*, *J. Am. Chem. Soc. 89*, 4190−4196.
67. Urry, D. W., and Pettegrew, J. W. (1967) Model systems for interacting heme moieties. II. The ferriheme octapeptide of cytochrome *c*, *J. Am. Chem. Soc. 89*, 5276−5283.
68. Laberge, M., Vreugdenhil, A. J., Vanderkooi, J. M., and Butler, I. S. (1998) Microperoxidase-11: molecular dynamics and Q-band excited resonance Raman of the oxidized, reduced and carbonyl forms, *J. Biomol. Struct. Dyn. 15*, 1039−1050.
69. Blauer, G., Sreerama, N., and Woody, R. W. (1993) Optical activity of hemoproteins in the Soret region. Circular dichroism of the heme undecapeptide of cytochrome *c* in aqueous solution, *Biochemistry 32*, 6674−6679.
70. Othman, S., Lirzin, A. L., and Desbois, A. (1993) A heme c-peptide model system for the resonance Raman study of c-type cytochromes: characterization of the solvent-dependence of peptide-histidine-heme interactions, *Biochemistry 32*, 9781−9791.
71. Mazumdar, S., Medhi, O. K., and Mitra, S. (1991) Stability and Characterization of Iron(III) and Iron(II) Heme Peptides Encapsulated in Aqueous Detergent Micelles: 1H NMR and UV−Vis Spectroscopic Studies, *Inorg. Chem. 30*, 700−705.
72. Wang, J. S., and van Wart, H. E. (1989) Resonance Raman characterization of the heme c group in *N*-acetyl microperoxidase-8: a thermal intermediate spin-high spin state mixture, *J. Phys. Chem. 93*, 7925−7931.
73. Anfinrud, P. A., Lim, M., and Jackson, T. A. (1994) Femtosecond IR spectroscopy: methods and applications to protein dynamics, *Proc. SPIE 2138*, 107−115.
74. Wei, Y. Z., Kumbharkhane, A. C., Sadeghi, M., Sage, J. T., Tian, W. D., Champion, P. M., Sridhar, S., and Mcdonald, M. J. (1994) Protein hydration investigations with high-frequency dielectric-spectroscopy, *J. Phys. Chem. 98*, 6644−6651.
75. Rousseau, D. L., and Friedman, J. M. (1988) Transient and Cryogenic Studies of Photodissociated Hemoglobin and Myoglobin, in *Resonance Raman Spectra of Heme and Metalloproteins* (Spiro, T. G., Ed.) pp 133−215, John Wiley & Sons, Inc., New York.
76. Cao, W. (2003) Laser Flash Photolysis and Resonance Raman Investigations of Ligand Rebinding to Heme Proteins, Ph.D. Dissertation, Northeastern University, Boston, Massachusetts.
77. Hori, H., and Kitagawa, T. (1980) Iron-Ligand Stretching Band in the Resonance Raman Spectra of Ferrous Iron Porphyrin Derivatives. Importance as a Probe Band for Quaternary Structure of Hemoglobin, *J. Am. Chem. Soc. 102*, 3608−3613.
78. Teraoka, J., and Kitagawa, T. (1981) Structural Implication of the Heme-linked Ionization of Horseradish Peroxidase Probed by the Fe−Histidine Stretching Raman line, *J. Biol. Chem. 256*, 3969−3977.
79. Kincaid, J., Stein, P., and Spiro, T. G. (1979) Absence of heme-localized strain in T state hemoglobin: insensitivity of heme-imidazole resonance Raman frequencies to quaternary structure, *Proc. Natl. Acad. Sci. U.S.A. 76*, 549−552.
80. Nagai, K., Kitagawa, T., and Morimoto, H. (1980) Quaternary structures and low-frequency molecular vibrations of haems of deoxy and oxyhaemoglobin studied by resonance Raman scattering, *J. Mol. Biol. 136*, 271−289.
81. Ye, X. (2003) Ultrafast Photophysical and Photochemical Studies of Heme Proteins, Ph.D. Dissertation, Northeastern University, Boston, Massachusetts.
82. Sugimoto, T., Unno, M., Shiro, Y., Dou, Y., and Ikeda-Saito, M. (1998) Myoglobin mutants giving the largest geminate yield in CO rebinding in the nanosecond time domain, *Biophys. J. 75*, 2188−2194.
83. Bangcharoenpaurpong, O., Schomacker, K. T., and Champion, P. M. (1984) A resonance Raman investigation of myoglobin and hemoglobin, *J. Am. Chem. Soc. 106*, 5688−5698.
84. Li, X. Y., and Spiro, T. G. (1988) Is Bound CO Linear or Bent in Heme Proteins? Evidence from Resonance Raman and Infrared Spectroscopic data, *J. Am. Chem. Soc. 110*, 6024−6033.
85. Ray, G. B., Li, X. Y., Ibers, J. A., Sessler, J. L., and Spiro, T. G. (1994) How far can proteins bend the FeCO unit: distal polar and steric effects in heme-proteins and models, *J. Am. Chem. Soc. 116*, 162−176.
86. Vogel, K. M., Kozlowski, P. M., Zgierski, M. Z., and Spiro, T. G. (1999) Determinants of the FeXO (X=C,N,O) Vibrational Frequencies in Heme Adducts from Experiment and Density Functional Theory, *J. Am. Chem. Soc. 121*, 9915−9921.

BI0497291